Assessment of Large Eddy Simulation for the prediction of recessed inner tube coaxial flames

Thomas Schmitt

Assessment of Large-Eddy Simulation for the prediction of recessed inner-tube coaxial flames

Thomas Schmitt[1*]

[1*]Laboratoire EM2C, CNRS, CentraleSupélec, Université Paris-Saclay, 3, rue Joliot Curie 91192 Gif-sur-Yvette, France.

Corresponding author(s). E-mail(s): thomas.schmitt@centralesupelec.fr;

Abstract

Large Eddy Simulations of recessed central-duct coaxial injectors under transcritical and two-phase conditions are detailed in this paper, with the objective of assessing the ability of recently develop models [1, 2] to recover the experimental observations of an augmentation of the flame expansion rate and its dynamics due to the recess. The simulated cases correspond to the LOx/GH_2 Mascotte A10 and C10, both operating at 10 bar with two-phase flow conditions, and Mascotte C60, injected under transcritical conditions in a chamber at 60 bar [3]. Cases A10 and C10 qualitatively reproduce the experimental visualizations. However, the simulation with recess for case C60 produces a more disrupted inner jet and a shorter flame than in the experiment. In addition, a fine grid resolution is necessary to capture the absolute instability in this case. Case C60 is then examined. It is observed in particular that heat release rate distribution is importantly modified once the LOx injector is recessed, nearly doubled up to 10 LOx injector diameters. This huge increase of heat release has two origins: 1) an enhanced turbulent mixing in the near injector region due to an increased injector exit velocity because of the thermal expansion in the recessed part, in line with the model proposed by Kendrick et al. [4] ; 2) a larger flame surface because of the quicker destabilization and larger spreading rate of the flame at the injector exit.

Keywords: Large-Eddy Simulation, Liquid rocket coaxial injector, transcritical flow, two-phase flow

1 Introduction

Important progresses have been achieved in the last decade concerning the numerical modeling and the Large Eddy Simulation (LES) of cryogenic coaxial flames, like those encountered in liquid rocket engines [5–10]. In particular, LES now allows a good representation of single cryogenic coaxial flames operating at supercritical pressure [1, 11, 12] and encouraging results have been obtained on more complex configurations [13–15] and at subcritical pressure [2]. To the author's knowledge, the numerical assessment of the solvers has been so far restricted to configurations without recess of the the LOx tube, i.e. geometries in which the LOx injector exit is aligned with the hydrogen injector exit. However, actual rocket injectors generally feature recessed LOx injectors. This geometrical change is known to improve combustion efficiency, augmenting the flame expansion rate [4, 16]. This phenomenon is first attributed to an acceleration of the outer stream because of the volumetric expansion generated by the flame in the recessed part of the injector [4, 16]. It is also found that recess favors the development of long wavelength instabilities [17]. The confined wake becomes globally unstable, while the flow in the absence of recess is only convectively unstable or marginally absolutely unstable. The global instability of the recessed flow aids rupture of the liquid jet and enhances mixing of the gas and liquid flows downstream.

Large-Eddy Simulations (LES) of recessed coaxial injectors are reported in this article. The main objective of this work is to assess the ability of LES to properly reproduce the experimental observation. It is also of interest to identify the ressources needed to properly simulate such configurations with LES. The three configurations investigated here correspond to the LOx/GH_2 Mascotte A10, C10 and C60 case operating at 10 bar and 60 bar [3, 4, 16, 18], on which experimental tests with and without recess are available, in particular through experimental OH*-emission visualizations for the three cases [4, 16] and backlighting images for case C60 [16]. It was found the inner dense LOx stream features large scale oscillations when the LOx tube is recessed. A flow pattern not observed when the injector is not recessed.

The paper is organized as follow. The experimental configuration is first described in Sec. 2. The models and the numerical approach are then detailed in Sec. 3. A statistical and mesh convergence study is proposed in Sec. 4 and 5. Numerical results are then compared with experimental visualisations in Sec. 6. Finally, a discussion on the effect of recess is offered in Sec. 7.

2 Experimental reference case, computational domain and injection conditions

The experimental setup simulated in this paper corresponds to the single injector configuration of the Mascotte test-bench [3, 18]. Low-velocity liquid oxygen surrounded by high-velocity gaseous hydrogen are injected through a coaxial injector in the chamber at 10 bar and 60 bar. The injection conditions of

interest correspond to the cases A10, C10 and C60 in [16]. They are detailed in Tab. 1, in which P is the chamber pressure, $\dot{m}$ is the mass flow rate at O_2 and H_2 inlets, u_{inj} the injection velocities and $J=(\rho_{H_2} u_{H_2}^2)/(\rho_{O_2} u_{O_2}^2)$ is the momentum flux ratio between the hydrogen and oxygen jets. For all the cases, the injection temperatures T_{inj} are set to 80 K for oxygen and 288 K for hydrogen. Under such conditions, both reactants are injected at supercritical pressure and the injection is in this study considered as transcritical for case C60 while the cases at 10 bar are at subcritical pressure for the oxygen and the flow is two-phase.

Table 1 Injection conditions used in the simulations.

Case	P [bar]	$\dot{m}_{O_2}$ [g/s]	$\dot{m}_{H_2}$ [g/s]	u_{inj,O_2} [m/s]	u_{inj,H_2} [m/s]	J
A10	10	50	23.7	2.6	300	14.5
C10	10	50	15.8	2.6	195	6.5
C60	60	100	45	5.2	160	6.8

The computational domain is shown in Fig. 1 and reproduces the geometry of the experimental chamber, but without the exit nozzle. The domain features a square-shaped section (50 mm x 50 mm) combustion chamber and its length is 500 mm. Two injector arrangements are considered in this study (Fig. 2). Cases NR include a flush mounted inner injector while in cases R, the LOx tube has a recess length r equal to 1d [4, 16], d being the LOx injector exit diameter.

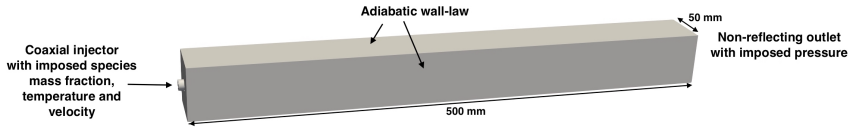

Fig. 1 Tri-dimensional visualization of the computational domain and boundary conditions.

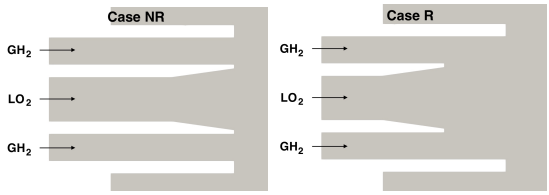

Fig. 2 Longitudinal cut of the coxial injector (here shown for case C60). Left: non recessed injector ; right: recessed injector.

3 Models and numerical strategy

3.1 Models and boundary conditions

The simulations performed in this work rely on the methodology detailed in [1] and [2]. It is here briefly recapped, more details can be found in the aforementioned references. The Favre-filtered fully compressible Navier-Stokes equations are solved in a Large-Eddy Simulations (LES) framework. The fluid viscosity and the heat diffusion coefficients are calculated following the Chung *et al.* method [19], and the species diffusion coefficients are obtained under the assumption of unity Lewis number. The Soret and Dufour effects are neglected. The sub-grid scale (SGS) stress tensor is modeled with the WALE model [20]. The SGS energy and species fluxes are considered using the gradient transport assumption with turbulent Prandtl and Schmidt numbers both set to 0.7.

Chemical conversion is handled using an infinitely fast chemistry model [1]. This model accounts for the following species: H_2, O_2, H_2O and OH, in order to properly calculates the burnt gas temperature. Equilibrium reference mass fractions are tabulated in terms of the mixture fraction Z and its variance $Z"^2$, both transported during the simulations. The filtered species source terms and heat release rate are then computed following the relaxation procedure described in [1].

Thermodynamic non-idealities are accounted for using the Soavre-Redlich-Kwong equation of state (EoS) [21], used for a consistent derivation of all thermodynamic coefficients and functions [22]. The thermodynamic model is shown to be accurate for the flow conditions under consideration (see [1] for more details). For the subcritical pressure cases at 10 bar, featuring a two-phase flow, the 3-equation homogenous equilibrium multi-fluid model from [2], assuming an approximate multi-species liquid / vapor equilibrium in thermodynamically unstable control volumes, is used. The approximate equilibrium consists in assuming that both phases have equal composition. Such an approximation is reasonable as long as phase separation is not dominated by a chemical instability [2].

The compressible unstructured solver AVBP [23, 24] is used for this study. Its Taylor-Galerkin weighted residual central distribution scheme, called TTGC, is third-order in time and space [25]. Numerical stabilization uses artificial viscosity as described in [1]. Inlet and outlet boundaries are treated with the characteristic wave decomposition method NSCBC derived for non-ideal thermodynamics [2, 26]. Walls are treated using adiabatic slip wall-law boundary condition [27, 28]. Heat losses at the chamber walls may possibly impact the whole flame, however this aspect has not been treated here, as being out of the scope of this study.

3.2 Meshing strategy

An adaptative mesh refinement technique is used in this work. It is based on the method developed by Daviller et al. for AVBP [29], based on the MMG3D

library of Dapogny et al. [30]. The concept is to refine the mesh in regions where given quantities are poorly resolved. This is done in a static way: the refined mesh is built using averaged solutions. The method is repeated until a mesh convergence is obtained (this aspect is discussed in Sec. 5). As the refinement criteria used in this work differ from the one proposed in [29], they are detailed below. The less resolved regions of the flow are detected using a gaussian filter:

$$G^{\phi}(x,y,z) = \| < \widehat{\phi}(t,x,y,z) > - < \phi(t,x,y,z) > \| \tag{1}$$

where $< \cdot >$ denotes temporally averaged data and $\widehat{\cdot}$ indicates a spatial gaussian filtering. Note that in practice, this gaussian filter is approximated by a second order derivative [31]:

$$G^{\phi}(x,y,z) \approx \frac{\Delta_x^2}{2} \| \nabla \cdot \nabla (< \phi(t,x,y,z) >) \| \tag{2}$$

where Δ_x is the characteristic cell size. As the objective is to properly retrieve the flow dynamics and the flame topology, the criteria is based on the velocity $\phi^u = \sqrt{u^2+v^2+w^2}$, the sound speed $\phi^c = c$, with c the sound speed, and the heat release rate $\phi^{\omega} = \dot{\omega}_T$, with $\dot{\omega}_T$ the heat release rate.

Then, for a given flow variable ϕ, a mesh scaling factor f^{ϕ} is defined [29]:

$$f^{\phi}(x,y,z) = \left(1 - \frac{\overbrace{G^{\phi}(x,y,z)}^{} - G^{\phi}_{min}}{G^{\phi}_{max} - G^{\phi}_{min}} \right) (1-\epsilon) + \epsilon \tag{3}$$

where ϵ determines the smallest scaling factor (sets to 0.5 here) and G^{ϕ}_{min} and G^{ϕ}_{max} are respectively the minimum and maximum values of G^{ϕ} in the domain. The overbrace $\overbrace{\cdot}$ indicates that the variable is filtered applying 5 times the approximate Gaussian filter detailed in Eq. 2. This smooths the field to make it more homogeneous and removes possible localized oscillations that may pollute the final criteria.

The final local mesh scaling factor $F(x,y,z)$ is computed first by taking the minimum between the ones built from the different flow variables, $F = \min(f^u, f^c, f^{\omega})$, and then by applying a sequence of propagations of the smallest factor over 5 cells in order to avoid any confinement by the grid.

3.3 Meshes and simulated cases

The initial mesh, referred to as M0, is shown in Figs. 3a and 4a. Inlets are meshed with 10 cells in the hydrogen stream and 17 cells in the oxygen flow. The characteristic cell size is constant in the near injector region, except near the injector lip, where it is refined to ensure at least 3 cells behind the lip (Fig. 4a). The mesh is then coarsened further downstream. It contains 650 000

nodes and 3 500 000 tetrahedra (Tab. 2). The mesh is then refined several times following the procedure depicted in Sec. 3.2, leading to meshes M1, M2 and M3 obtained after 1, 2 and 3 refinement iterations, respectively. Resulting meshes are shown in Figs. 3bc and 4bc. The cell size is essentially reduced in the injector region and in particular in the annular stream and behind the lip. Tab. 2 details the meshes characteristics. Note that the mesh characteristics of the recessed and non recessed geometries are very similar, thus only the injector with recess is shown here. Similarly, details given in this table are for case C60, as differences with cases C10 and A10 are small. The associated CPU cost (on AMD Rome (Epyc) processors running at 2.6 GHz) increases quickly with the refinement iterations and mesh M2 is about 100 times more expensive than M0.

Table 2 Details of the meshes used for the simulation. Δ_t is the time step during the simulation. "kh" stands for kilo CPU hours. M0, M1, M2 and M3 are typically run on 1024, 4096, 8192 and 16384 cores on AMD Rome (Epyc) processors running at 2.6 GHz.

Mesh	Nb nodes	Cells LOx	Cells GH_2	Cells lips	Δ_t [ns]	CPU (10 ms) [kh]
M0	650 000	17	10	3	13.0	6.5
M1	2 500 000	20	20	6	6.5	76
M2	10 000 000	20	≈30	12	3.0	650
M3	40 000 000	20	≈40	24	1.3	4 600

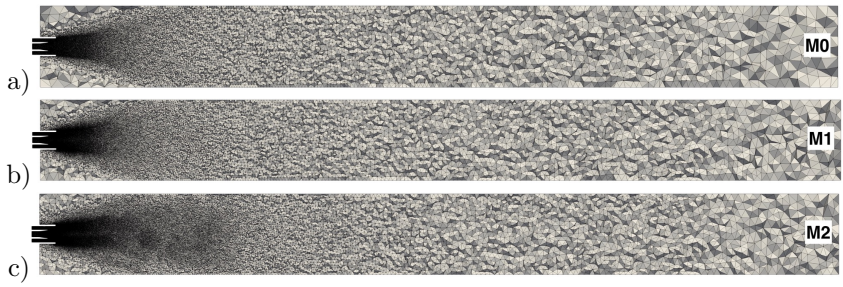

Fig. 3 Longitudinal slices of the 3 meshes (case C60 with recess). Top: initial mesh M0, middle: mesh M1 and bottom: mesh M2.

Simulated cases are summarized in Tab. 3. The first part of the acronym corresponds to the experimental conditions, A10, C10 or C60. Cases are referred as "-NR" for the injector without recess and "-R" for the simulations with a 1d-recessed LOx tube. The associated grid is given by the case number. Simulations are started on the coarser grid (M0) with an initially uniform domain filled with hydrogen at its injection temperature. Once convergence is reached, the mesh is adapted following the procedure described in Sec. 3.2 and the last solution is interpolated on the new grid. The procedure is repeated for the successive mesh refinements performed in this work. Statistics are gathered during a time τ_{av} after a transient time $\tau_{transient}$ (to ensure the flow

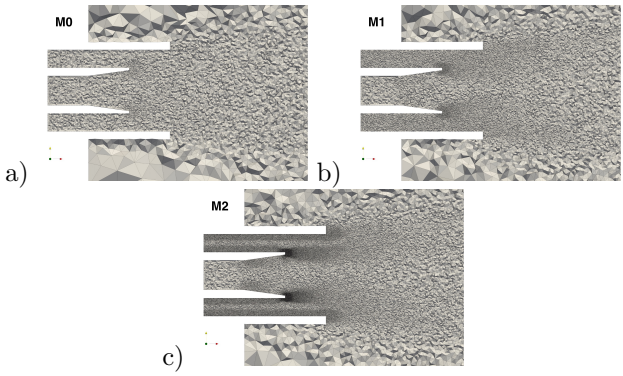

Fig. 4 Longitudinal slices of the 3 meshes in the injector region (cases with recess). Top: initial mesh M0, middle: mesh M1 and bottom: mesh M2.

is properly converged). These times could be compared with the convective time defined by $\tau_{conv} = \int_0^{60d} 1/u_{centerline}(x)dx \approx 30$ ms, 60d being the length of interest for the comparisons with experiments and between the cases and $u_{centerline}$ the axial velocity along the inner jet centerline. Despite the larger injection velocity for the cases C60, τ_{conv} is eventually similar for all the cases due to the presence of a low velocity region around 15d for the latter cases. The oxygen injection velocity is used here as it is the lowest velocity at injection. It is thus expected that this convective time is the limiting one. At least one convective time is used for τ_{av} for meshes M0 and M1 for cases A10, C10 and C60 and for mesh M2 for cases C60. The issue of statistical convergence is investigated more in detail in Sec. 4. Finally, case C60-R3, which is very expensive, and case C10-R2 are only used for a study in the recessed part, justifying their small averaging times, since one through time of the LOx stream in the recessed part is estimated to be around 1 ms for case C60 and 2 ms for case C10. Similarly, case A10-R2, with only 10 ms of averaging time, is restricted to a comparison in the near injector region, up to 10d.

Table 3 Simulated cases. The averaging time used for statistics is given by τ_{av} and $\tau_{transient}$ is the transient time before averaging is started.

Case	Exp. conditions	Recess	Mesh	τ_{av} [ms]	$\tau_{transient}$ [ms]
A10-R0	A10	1d	M0	60	30
A10-R1	A10	1d	M1	60	30
A10-R2	A10	1d	M2	10	10
A10-NR1	A10	0	M1	30	30
C10-R0	C10	1d	M0	60	30
C10-R1	C10	1d	M1	60	30
C10-R2	C10	1d	M2	6	3
C10-NR1	C10	0	M1	30	30
C60-R0	C60	1d	M0	60	40
C60-R1	C60	1d	M1	60	40
C60-R2	C60	1d	M2	30	10
C60-R3	C60	1d	M3	2.7	1.5
C60-NR2	C60	0	M2	36	30

4 Statistical convergence

The influence of the averaging time is investigated here. We will concentrate on cases with recess as conclusions are similar with the other geometry and cases. Statistical convergence in the recess for cases A10-R2, C10-R2 and C60-R3 is shown in Annex A. Radial profiles of temperature and axial velocity for different averaging times are shown in Figs. 5 and 6, Figs. 7 and 8 and Figs. 9 and 10 for case A10-R1, C10-R1 and C60-R2, respectively.

Results for 30 ms and 60 ms are very close from each other, for both cases A10-R1 and C10-R1. It indicates that 30 ms is a proper averaging time for these cases, as suggested in Sec. 3.3 from the estimation of the convective time, and that a good statistical convergence is achieved.

For case C60-R2, it is found that results between 20 ms and 30 ms are very close from each other, both in terms of mean and rms data. The statistical convergence is thus considered as achieved for case C60-R2.

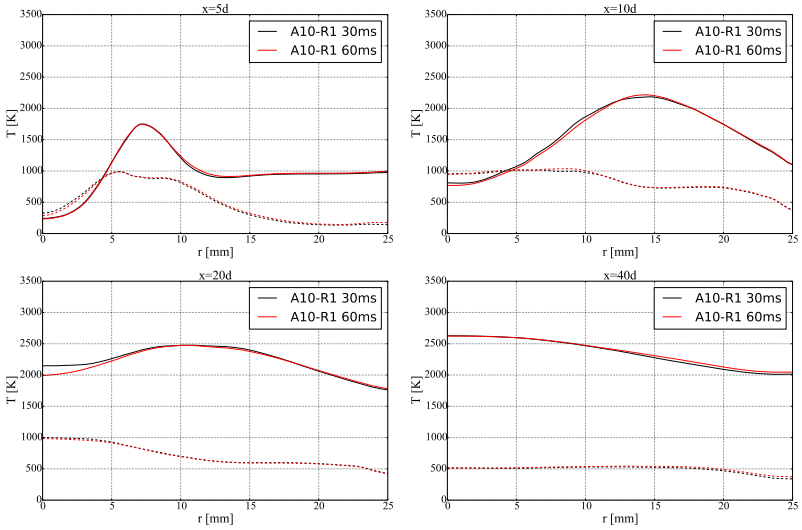

Fig. 5 Case A10-R1, statistical convergence. Radial profiles of temperature. − mean profiles, −− rms profiles.

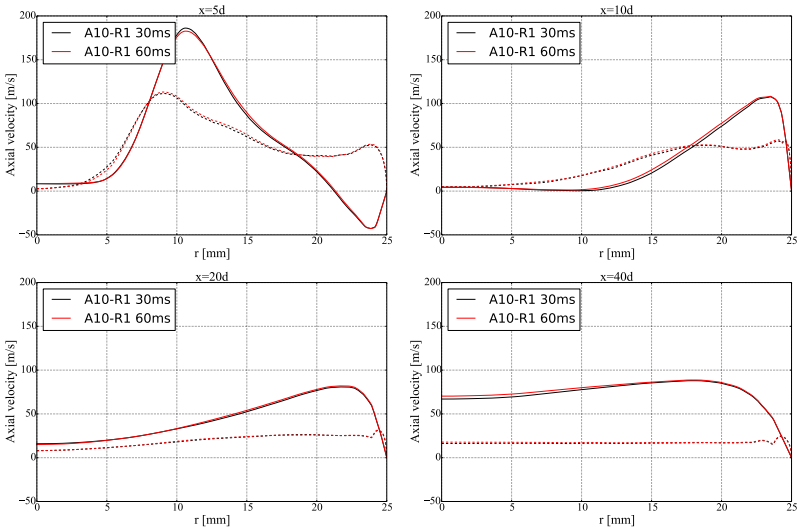

Fig. 6 Case A10-R1, statistical convergence. Radial profiles of axial velocity. − mean profiles, −− rms profiles.

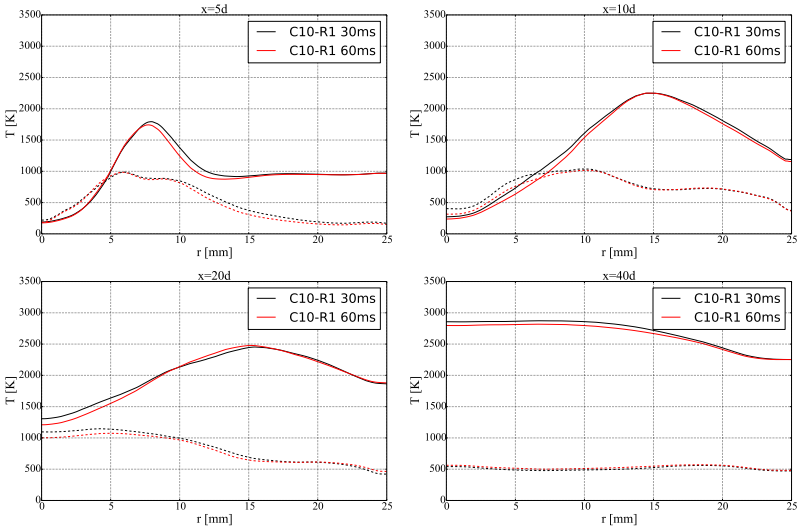

Fig. 7 Case C10-R1, statistical convergence. Radial profiles of temperature. − mean profiles, −− rms profiles.

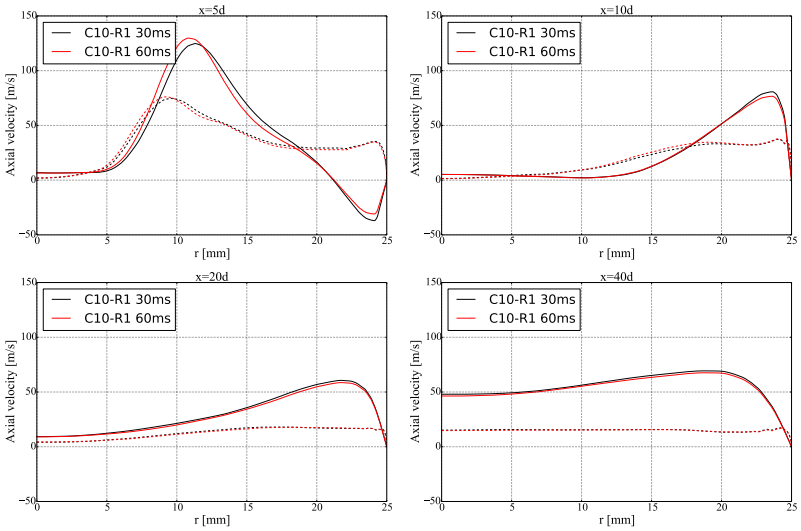

Fig. 8 Case C10-R1, statistical convergence. Radial profiles of axial velocity. − mean profiles, −− rms profiles.

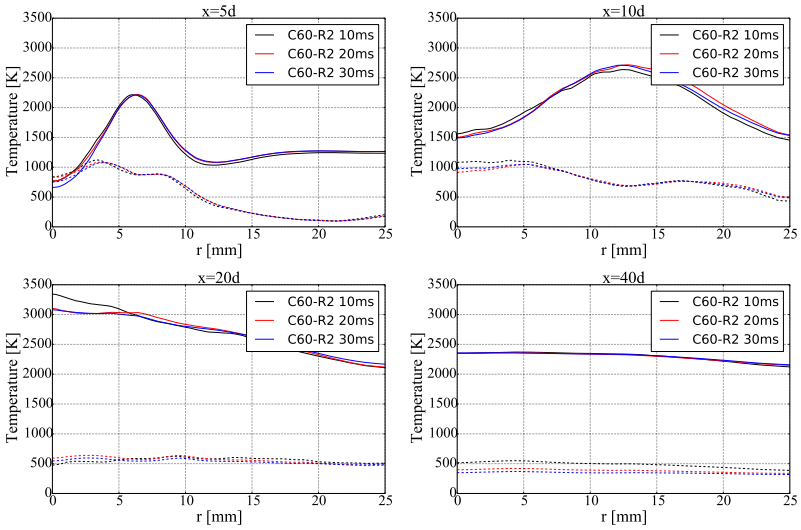

Fig. 9 Case C60-R2, statistical convergence. Radial profiles of temperature. − mean profiles, −− rms profiles.

5 Mesh convergence

The influence of the grid resolution is studied in this section. Proper results should provide mean quantities that are independent of the mesh. Mesh convergence is shown here for the recessed cases A10-R, C10-R and C60-R.

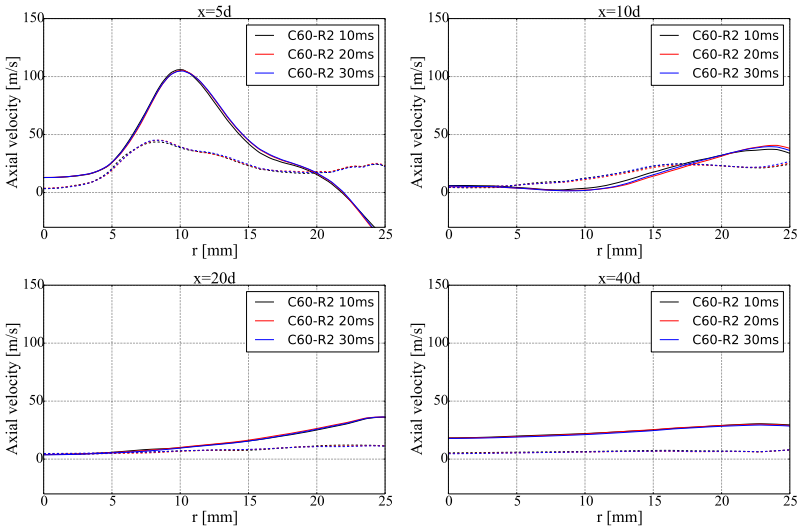

Fig. 10 Case C60-R2, statistical convergence. Radial profiles of axial velocity. − mean profiles, −− rms profiles.

5.1 Case C10-R

Longitudinal slices of mean oxygen mass fraction, temperature and axial velocity are shown in Fig. 11 for cases C10-R0 and C10-R1. The initial opening of the flame is similar for both meshes. Also, for both cases, the oxygen penetrates the chamber up to 35d, indicating the two flames have the same length.

This is confirmed by the longitudinal profiles of transversally averaged temperature and velocity plotted in Fig. 12. The sudden increases of temperature corresponds to the region where the flow interacts with the walls and the inner jet destabilizes. The two grids predict the same evolution of the mean temperature and axial velocity.

Finally, in order to follow a similar methodology than for case C60 (detailed in Sec. 5.3), an additional grid refinement is performed. Because this case is CPU demanding, the analysis is restricted to the recessed region. The latter is expected to be the most critical region where the instability should be captured and will determine the rest of the flame dynamics. Radial profiles of temperature, axial velocity and oxygen mass fraction for case C10-R2 are plotted in Figs. 13 to 15. The profiles for case C10-R0 are slightly shifted compared with the ones from cases C10-R1 and C10-R2, but their shapes are similar. Very close results are obtained for cases C10-R1 and C10-R2: mean and rms profiles are similar. From all the analysis presented in this section, it is concluded that simulation results are independent of the grid resolution for mesh M1 and allow a proper comparison with the experimental visualizations.

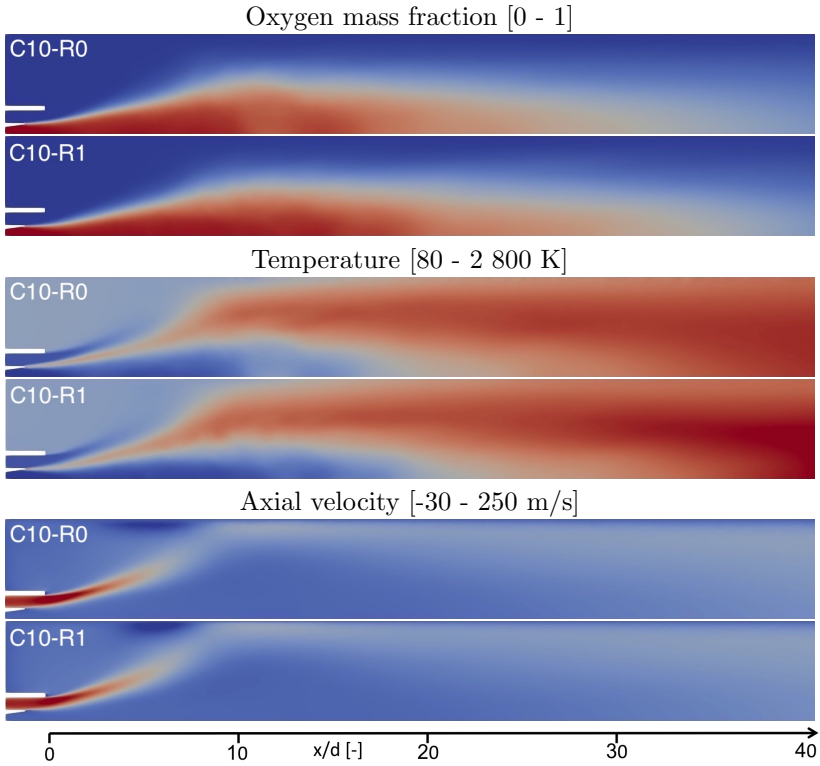

Fig. 11 Cases C10-R, mesh convergence. Longitudinal slices of averaged oxygen mass fraction, temperature and axial velocity for cases C10-R0 and C10-R1.

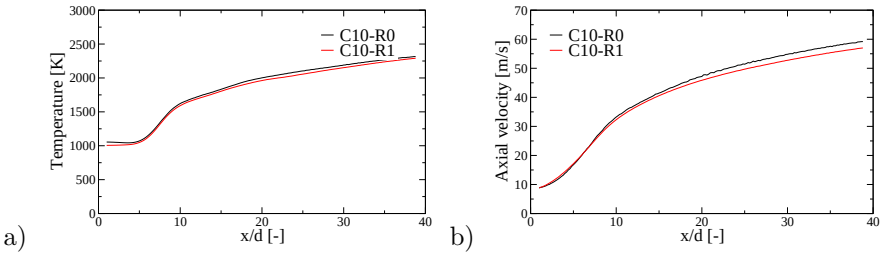

a) b)

Fig. 12 Cases C10-R, mesh convergence. Transversally averaged (a) temperature and (b) axial velocity.

5.2 Case A10-R

Similarly than for C10-R, longitudinal slices of mean oxygen mass fraction, temperature and axial velocity are shown in Fig. 16 for cases A10-R0 and A10-R1. While the initial spreading rate of the flame is close for the two grids, A10-R1 seems to produce a flame (looking at the oxygen mass fraction field for example) that is longer than A10-R0. Also, the temperature field is more diffused after 10d for case A10-R0 than for case A10-R1.

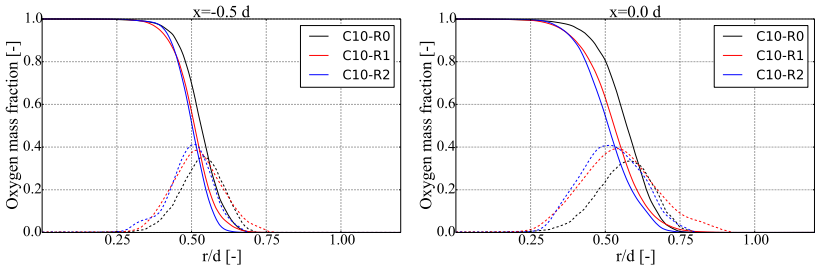

Fig. 13 Cases C10-R, mesh convergence. Radial profiles of oxygen mass fraction. − mean profiles, −− rms profiles.

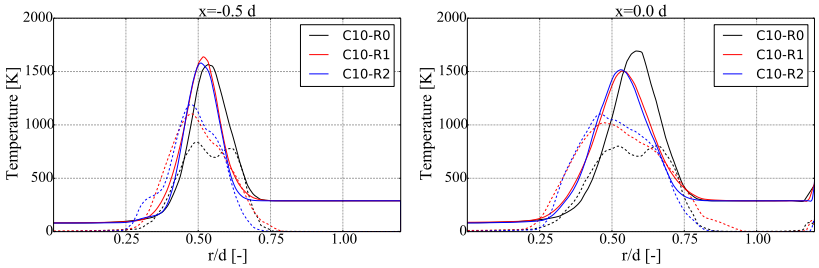

Fig. 14 Cases C10-R, mesh convergence. Radial profiles of temperature. − mean profiles, −− rms profiles.

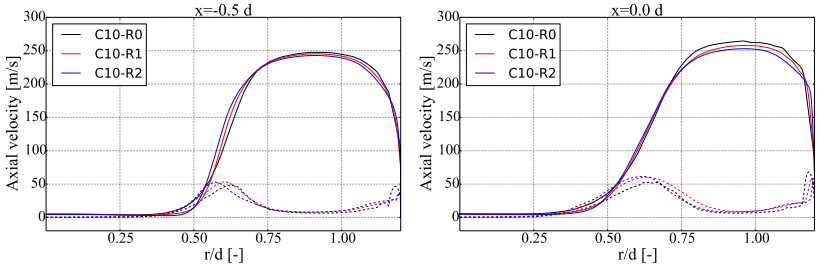

Fig. 15 Cases C10-R, mesh convergence. Radial profiles of axial velocity. − mean profiles, −− rms profiles.

The departures observed with the longitudinal slices are also present in the longitudinal profiles of transversally averaged temperature and velocity (Fig. 17). An additional grid refinement is then considered, case A10-R2. Given the simulation time for the later case, comparison is limited to 10d, but is sufficient to see that the flame spreading occurs at the same axial position (≈10d) between cases A10-R1 and A10-R2. Moreover, temperature and velocity increases are similar between the two cases.

The convergence in the recessed region is plotted in Figs. 18 to 20. Cases A10-R1 and A10-R2 have similar mean and rms profiles shape (slope, width or maximum), but the curves are not superimposed, slightly more eccentric

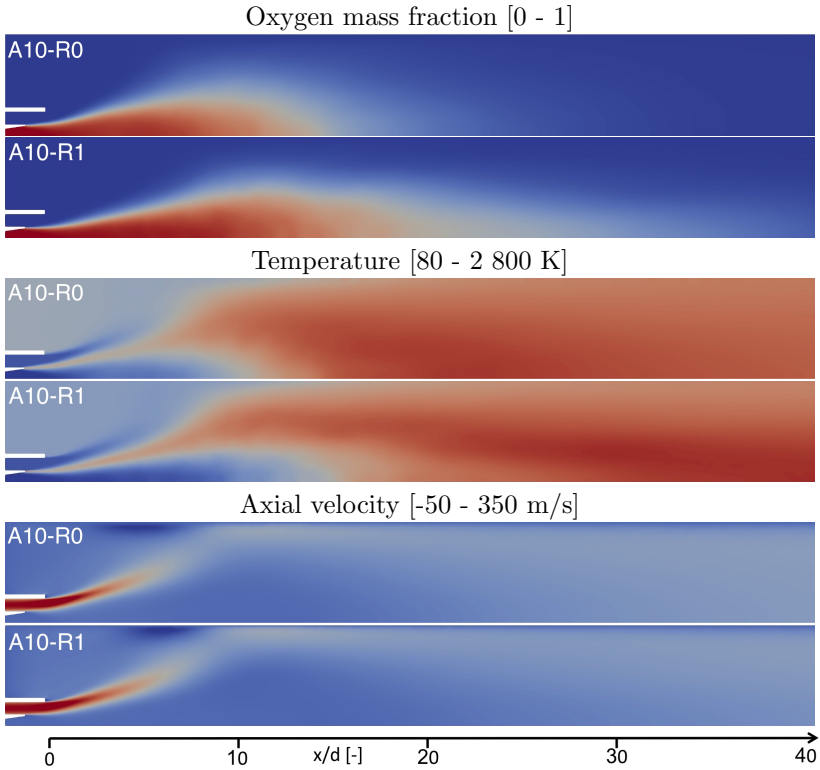

Fig. 16 Cases A10-R, mesh convergence. Longitudinal slices of averaged oxygen mass fraction, temperature and axial velocity for cases A10-R0 and A10-R1.

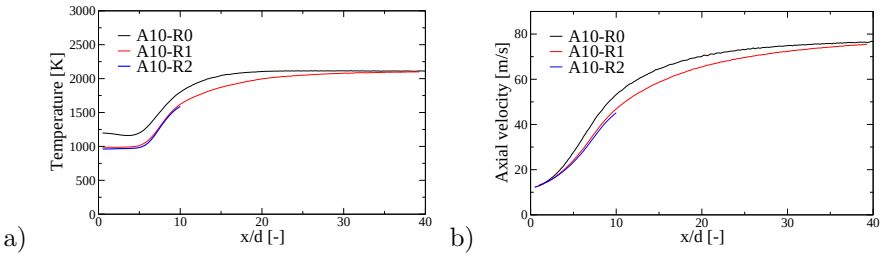

Fig. 17 Cases A10-R, mesh convergence. Transversally averaged (a) temperature and (b) axial velocity.

for A10-R1. Based on all the comparisons made in this section, it is expected that the departure between R1 and R2 in the recess part will not affect the whole flame dynamics and convergence is considered sufficient with mesh M1 for the study proposed in this work.

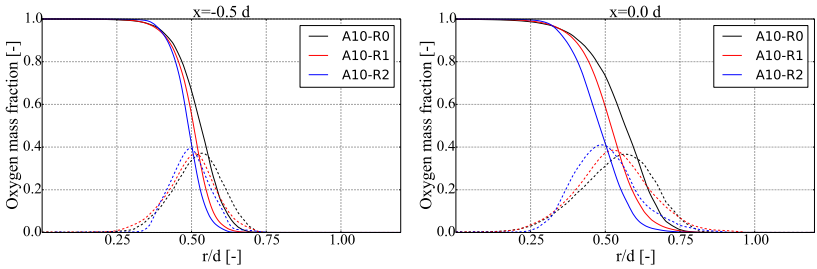

Fig. 18 Cases A10-R, mesh convergence. Radial profiles of oxygen mass fraction. — mean profiles, –– rms profiles.

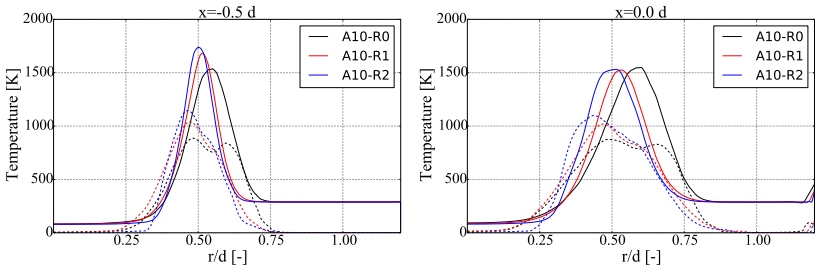

Fig. 19 Cases A10-R, mesh convergence. Radial profiles of temperature. — mean profiles, –– rms profiles.

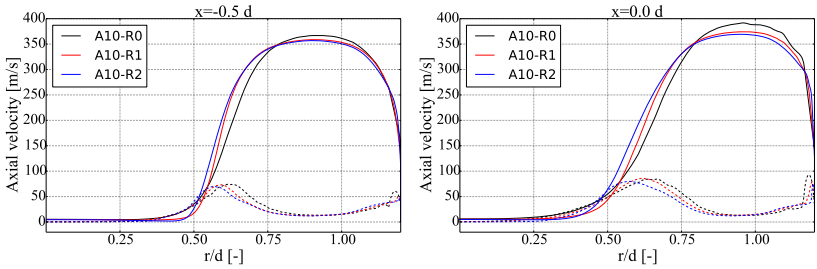

Fig. 20 Cases A10-R, mesh convergence. Radial profiles of axial velocity. — mean profiles, –– rms profiles.

5.3 Cases C60-R

Mesh convergence is shown now for the recessed case at 60 bar. The longitudinal profiles of averaged temperature and axial velocity in Fig. 21 show that cases C60-R0 and C60-R1 give close results, even-though the transition observed around 10d occurs sooner for case C60-R0 than C60-R1. Case C60-R2 departs from the two other grids: the increase of temperature happens closer to the injector and the increase of axial velocity is stronger for case C60-R2 than C60-R1. Case C60-R2 predicts a shorter flame than the two other cases.

The sudden change of flame topology with the grid resolution is confirmed with longitudinal slices of oxygen mass fraction, temperature and axial velocity

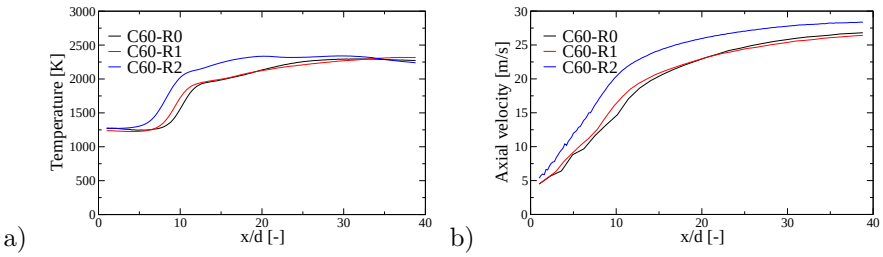

Fig. 21 Cases C60-R, mesh convergence. Transversally averaged (a) temperature and (b) axial velocity.

in Fig. 22. As the mesh is refined the flame spreading angle is increased and its length is strongly reduced. Interestingly, the departure between the cases seems to increase as the mesh is refined. From observations of the flow field, it seems unlikely that this phenomenon is due to insufficient mesh resolution in the chamber, but it is rather associated with a false reproduction of the natural instability in the recess. The mesh convergence study is then continued by performing another mesh refinement and focusing on the recessed part.

Radial profiles of oxygen mass fraction, temperature and axial velocity inside the injector, after the LOx tube exit at x=-0.5 d and x=0, are plotted in Figs. 23 to 25 for cases C60-R0, C60-R1, C60-R2 and C60-R3. As expected, case C60-R2 strongly departs from cases C60-R0 and C60-R1. Mean profiles of oxygen mass fraction and temperature are more diffused and the amplitude of rms fluctuations are larger for case C60-R2, suggesting a stronger dynamics in the recess for this case compared with C60-R0 and C60-R1. The refined mesh (case C60-R3) leads to results that are close to case C60-R2. In particular the shape of the mean profiles and the level of fluctuations are comparable between the two cases. It is concluded that cases C60-R0 and C60-R1 are not able to capture the expected absolute instability, contrary to cases C60-R2 and C60-R3. From this grid convergence study, it seems that mesh M2 is able to reasonably reproduce the dynamics of the flow and can thus be used confidently for the rest of the study.

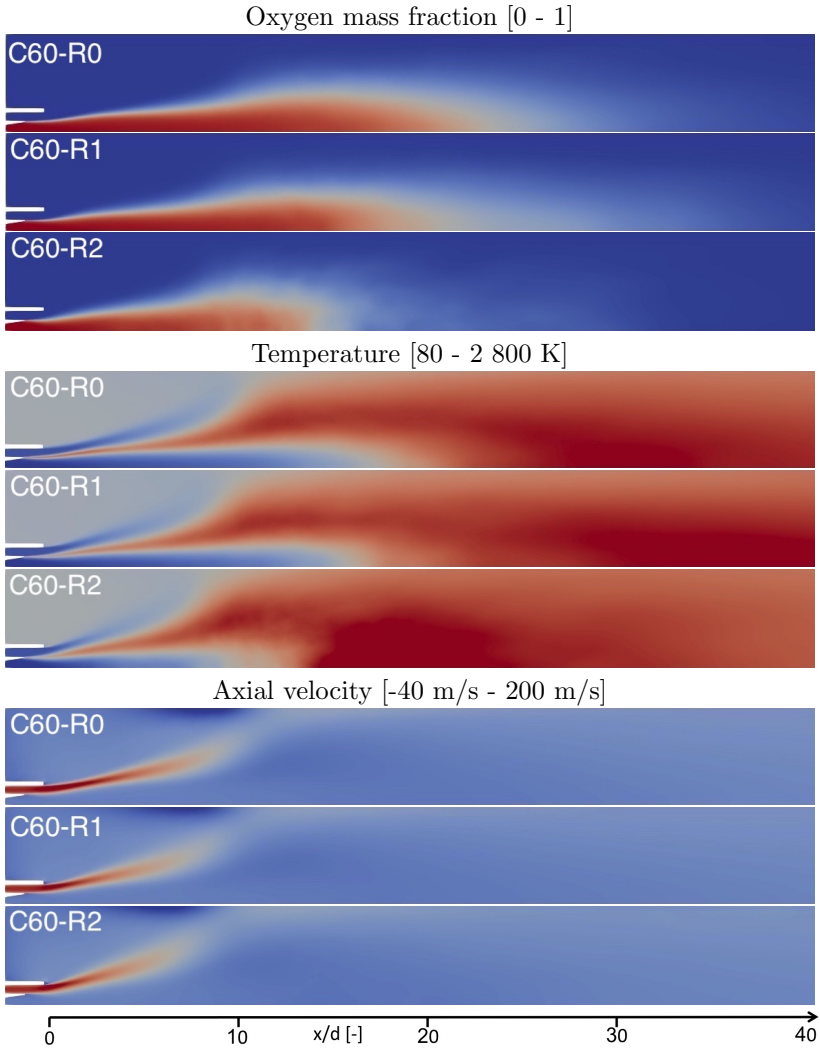

Fig. 22 Cases C60-R, mesh convergence. Longitudinal slices of averaged oxygen mass fraction, temperature and axial velocity for cases C60-R0, C60-R1 and C60-R2.

6 Comparison with experiments

6.1 Cases A10 and C10

To allow for a qualitative comparison of the mean flame position, mean OH mass fraction is compared with OH* emission visualizations for cases A10 and C10 in Fig. 26. The white dashed line represents the position of maximum OH* emission in the experiments from an average between the upper and lower part of the picture. The red dashed line shows the position of maximum OH

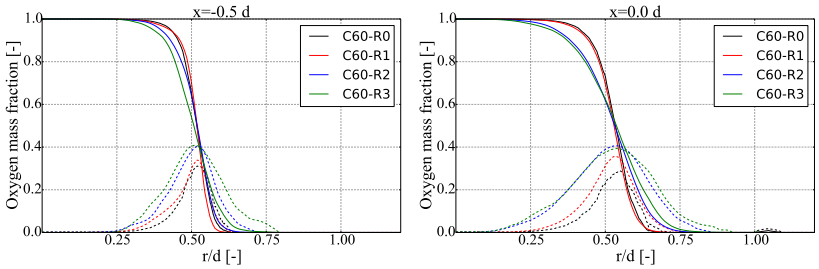

Fig. 23 Cases C60-R, mesh convergence. Radial profiles of oxygen mass fraction. — mean profiles, –– rms profiles.

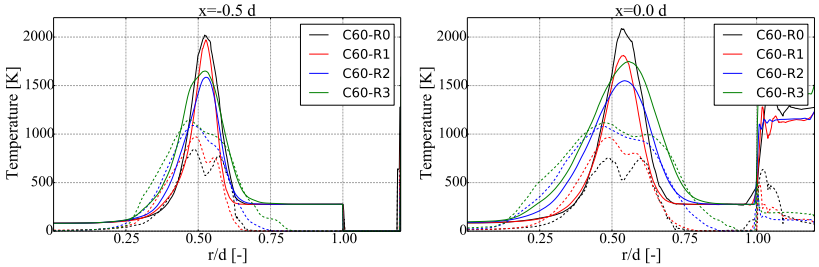

Fig. 24 Cases C60-R, mesh convergence. Radial profiles of temperature. — mean profiles, –– rms profiles.

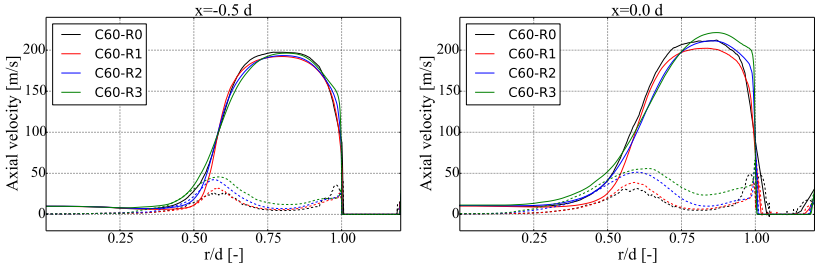

Fig. 25 Cases C60-R, mesh convergence. Radial profiles of axial velocity. — mean profiles, –– rms profiles.

mass fraction in the simulations. Flush mounted injector cases show a reasonable agreement with the experimental flame topology, even though both cases seem to lead to a little longer flame than in the experiment. There is also a departure directly at the injector exit for case C10, where the small pinch of the flow is not captured by the simulation. It is believed that this difference is due to an incorrect prediction of the flow separation in the tapered part of the LOx injector for this case. However, the overall agreement is satisfactory. Once the LOx injector is recessed, the initial opening of the flame is properly captured by the simulations. In particular, the nearly straight opening of the flame immediately at the injector exit, characteristic of these flames with recess,

is well retrieved. This suggests that the near injector dynamics are qualitatively reproduced. Moreover, the maximum radius axial position is reasonably recovered for both cases. The flames obtained with the recessed injector are slightly shorter than the ones without recess (the axial position of the maximum radius is decreased), and their initial expansion seems augmented, but differences remain limited.

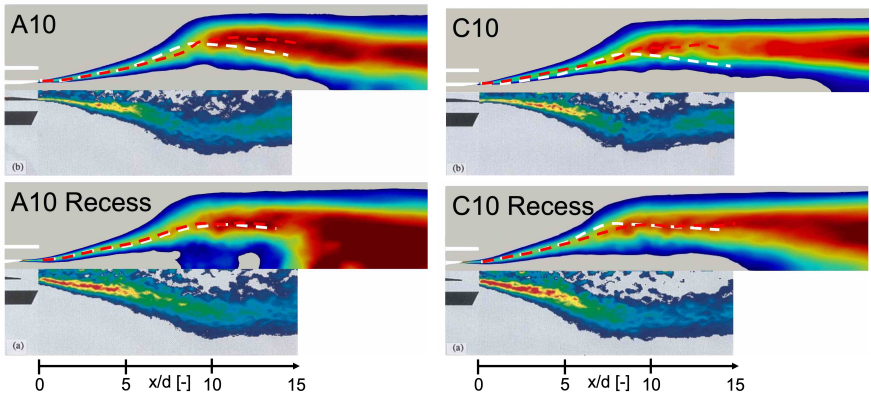

Fig. 26 Comparison with experiment, cases A10 and C10. Comparison between Abel transformed OH* mean emission images from experiments [4] and mean OH mass fraction from LES (between 0.01 and 0.05).

6.2 Cases C60

The flame topology from LES is now compared with experimental results from [16]. First, the mean flame position is analyzed. This is done in Fig. 27 by comparing experimental OH* emission pictures and OH mass fractions fields from LES for both the non recessed (left) and recessed cases (right). The white dashed line represents the position of maximum OH* emission in the experiments from an average between the upper and lower part of the picture. The case without recess is in agreement with the experimental visualization: the flame location and both the initial and final spreading rates are reasonably reproduced. However, the flame seems shorter in the simulation, the downstream spreading rate around $x \approx 11$d being different between the experiment and the simulation. There is no clear explanation for these discrepancies at the moment. It could be associated with the inlet turbulent injection profiles and intensity chosen in this work or the way solid boundaries are treated in the chamfer. Interestingly, case C60-R2 is in better agreement with the experimental visualization of Juniper et al. [32] operating under close conditions (not shown here). This is in line with similar simulations performed in [1]. The simulation with a recessed injector (Fig. 27 right) does not match as well the experimental picture. The spreading rate is over-estimated and the flame seems shorter. Such a discrepancy suggests that LES predicts a more intense

mixing of the LOx jet with the surroundings compared with the experiment. This is analyzed in the following.

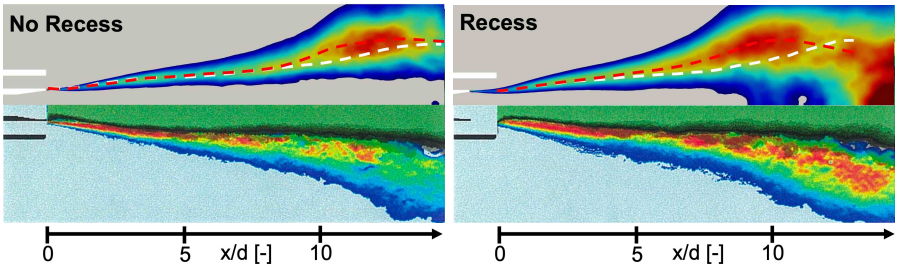

Fig. 27 Comparison with experiment, cases C60. Bottom: Mean backlighting and Abel transformed OH* emission images from experiments [16] ; Top: Mean OH mass fraction from LES (from 0.01 to 0.04). Left: non recessed injector, right: recessed injector.

The inner jet topology and dynamics are now qualitatively compared with experiments in Fig. 28, thanks to the experimental instantaneous backlighting images from [16]. These images show the dense oxygen jet and the regions containing steep refractive index gradients in the gas. The intensity of light defines the edge of the oxygen jet. Experimentally, the ducted oxygen jet features large scale oscillations that are not observed without recess. Our objective is a qualitative comparison that highlight the dynamics of the inner jet. It was found that instantaneous slices of oxygen mass fractions seem appropriate to that purpose. In agreement with the experiments, the inner jet of the non recessed case is weakly perturbed while the recessed case shows more dynamics. However, it seems that the numerical results feature much larger oscillation amplitudes than those from the experiments. The inner jet presents large scale transverse oscillations and breaks in large parcels. The jet penetration seems to be shorter than in the experiment. These dynamics could explain the larger spreading rate that is obtained in LES. There is no clear justification at the moment for the discrepancy between LES and experiments. However, this departure may originate from the usage of non-reflecting boundary conditions at inlet, not accounting for the actual acoustic response of the injection lines. Another possibility comes from the hypothesis of adiabatic walls in the injector. Accounting for heat losses in the injector and feeding lines may change the inflow conditions and possibility the resulting instability. Finally, the impact of turbulence at injection should be investigated and may influence the development of the instability.

7 Influence of recess

The impact of the recess on the flame topology and its dynamics is analyzed below on case C60-R2 and C60-NR2. In the following, these cases are simply referred as R and NR, respectively. A similar analysis is performed on cases A10 and C10 in Annex B and C. Mean fields are first compared in Sec. 7.1. The

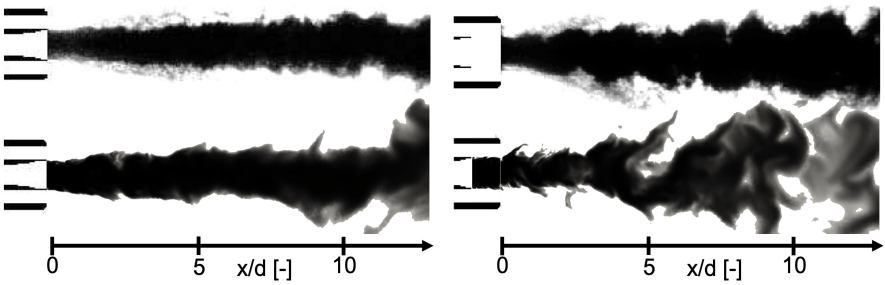

Fig. 28 Comparison with experiment, cases C60. Top: instantaneous backlighting images from experiments [16], bottom: instantaneous slice of oxygen mass fraction from the simulation (between 0.5 and 1).

dynamics are detailed in Sec. 7.2. Finally, the origin of the important increases of heat release rate due to the addition of the recess is discussed in Sec. 7.3.

7.1 Flame topology

The recess has a strong impact on the average flame shape. This is exemplified in Fig. 29, where longitudinal slices of mean temperature, density, oxygen mass fraction and axial velocity are shown. The initial spreading angle, measured using the radial position of the maximum temperature between x=0 and x=10d, is increased from 5.4° to 11.1° as the injector is recessed. The jet penetration is strongly reduced and the flame appears much shorter than without recess. This reduction is observed on all the variables shown here, i.e. temperature, density and oxygen mass fraction. The axial position of the maximum flame radius (measured here with the temperature field) is consequently lowered for the recessed case, passing from x=11.4d to x=9.9d.

This is analyzed more quantitatively in Fig. 30a with transversally averaged profiles of mean oxygen mass fraction. A flame length L_{O_2} can be defined based on the distance from the injector exit to the position at which the mean oxygen mass fraction is below 0.005, leading to L_{O_2}=36d and L_{O_2}=61d for cases R and NR, respectively. Accordingly, the heat release axial distribution is importantly changed. Near the injector exit, the heat release rate is approximatively doubled for case R. In the second part of the chamber (x>20d), the remaining unburned oxygen for case NR leads to an elongated profile of heat release, larger than for case R. Such modifications of heat release distribution may have important consequences for flame / acoustic interaction and combustion instabilities. The heat release rate is discussed more in detail in Sec. 7.3.

7.2 Flow dynamics

Instantaneous fields of temperature, density, oxygen mass fractions and axial velocity are shown in Fig. 31. Contrary to case NR, the flame formed with case R is strongly disrupted immediately at the injector exit. The inner core features a large amplitude transverse motion and finally breaks apart into large

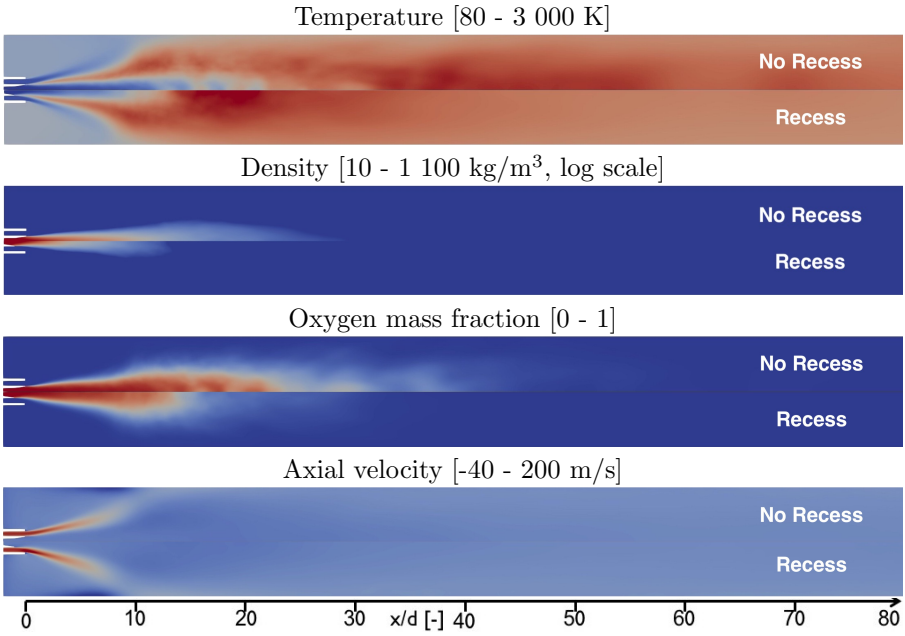

Fig. 29 No recess vs recess comparison. Longitudinal slices of average temperature, density, oxygen mass fraction and axial velocity. Blue: minimum, red: maximum.

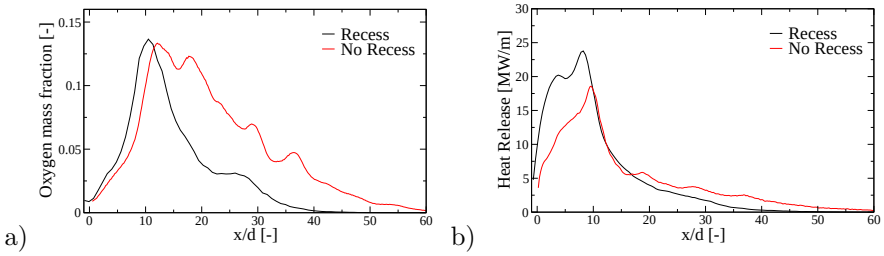

Fig. 30 No recess vs recess comparison. Longitudinal profile of transversely averaged oxygen mass fraction and transversely integrated heat release per unit length.

parcels. Footprints of the inner jet motion are visible on the annular stream velocity, regularly perturbed. This dynamics promote an augmented initial spreading rate of the flame.

The natural frequency of the instability is analyzed at the injector exit. Two probes are placed in the hydrogen and oxygen flows, at 0.5d from the injector exit (Fig. 32). Power spectral densities of axial velocity at probe H2 and of radial velocity at probe O2 are shown in Fig. 33, for both cases R and NR. As expected, the dynamics for case R is much stronger than for case NR, the red curve corresponding to case NR being barely visible because of its much lower amplitude than for case R. The instability is characterized by a large band response, and a dominant frequency around 1250 Hz.

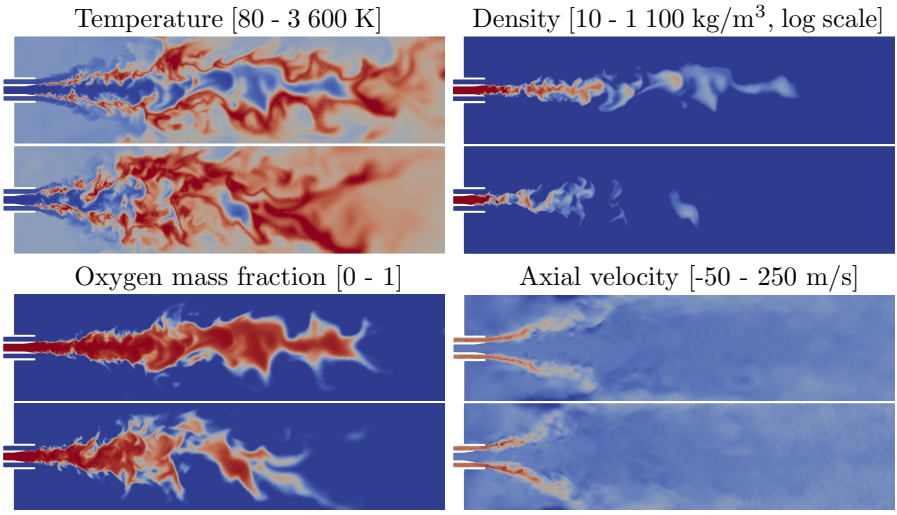

Fig. 31 No recess vs recess comparison. Longitudinal slices of instantaneous temperature, density, oxygen mass fraction and axial velocity. Blue: minimum, red: maximum.

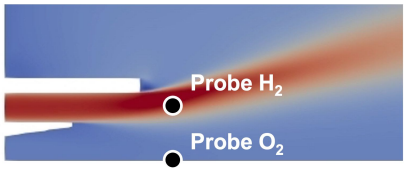

Fig. 32 No recess vs recess comparison. Position of the two probes used for dynamical study.

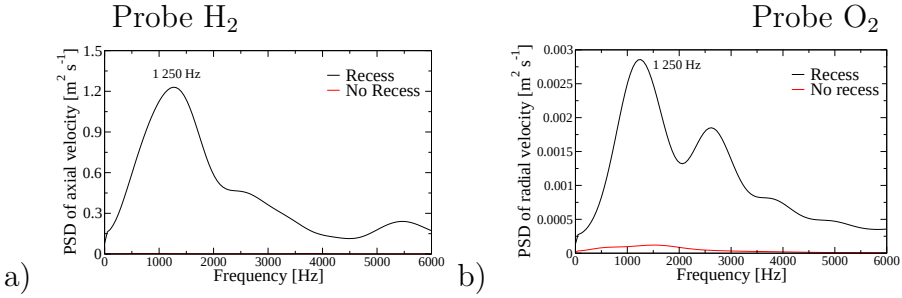

Fig. 33 No recess vs recess comparison. Power spectral density of (a) axial velocity in the annular stream and (b) radial velocity in the inner jet. A Welch's method is used, with 12 and 24 blocks for recessed and no recessed cases, respectively. The frequency resolution is 500 Hz.

7.3 Discussion

The addition of the recess on the LOx post leads to an important modification of the average heat release rate. To better characterize this phenomena, the mean heat release rate per unit length $\dot{q}_l$ plotted in Fig. 30b is decomposed as

follow:

$$\dot{q}_l(x) = \dot{q}_s(x)\Sigma_l(x) \tag{4}$$

In Eq. 4, $\dot{q}_s$ is the mean heat release rate per flame surface unit and $\Sigma_l(x)$ is the mean resolved flame surface per unit length. The latter is defined following [33] by $\Sigma_l(x) = \int_{S(x)} < \|\nabla \tilde{Z}(x,y,z,t)\| > dS$, with <> indicating a temporal averaging and $S(x)$ being the transverse surface at the axial position x. $\dot{q}_s$ is then obtained by dividing $\dot{q}_l$ by Σ_l. Σ_l and $\dot{q}_s$ as a function of the distance to the injector exit are plotted in Fig. 34 for the recessed and non recessed cases.

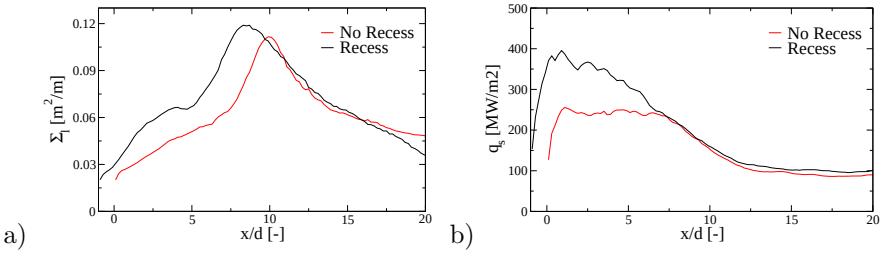

Fig. 34 No recess vs recess comparison. Longitudinal profile of (a) transversely integrated resolved flame surface per unit length and (b) transversely integrated heat release rate per resolved flame surface.

The resolved flame surface is importantly increased for case R compared with case NR, up to x=10d. This was expected because of the large amplitude motion of the inner jet induced by the instability observed previously in Sec. 7.2. Interestingly, the heat release rate per flame surface is also augmented close to the injector, up to x=7d. At the injector exit, $\dot{q}_s$ is approximatively doubled for case R compared with case NR.

In order to better understand the mechanism driving this increase at the injector exit, a set of radial profiles at x=0d for case R and x=1d for case NR are plotted in Fig. 35. The two profiles are not taken at the same axial position to account for the recess in the comparison and ensure similar resolved flame surfaces for the two cases, so that only $\dot{q}_s$ is responsible for the change in total heat release. As expected from the previous analysis, the heat release rate (Fig. 35a) is importantly augmented for r between 0.2d and 0.6d as the LOx tube is recessed. The mean oxygen mass fraction and density are modified accordingly, showing more diffused profiles for r<0.6d, while the profile of mean temperature is essentially shifted with larger values for r<0.5d. The level of oxygen mass fraction and temperature fluctuations is increased for r<0.5d.

An important departure is noticed concerning the mean axial velocity, plotted in Fig. 36. The latter is strongly increased for case R for r<1d. This is in line with the analytical work presented in [4]. It suggests that the thermal expansion due to the combustion in the recessed, confined, part of the injector

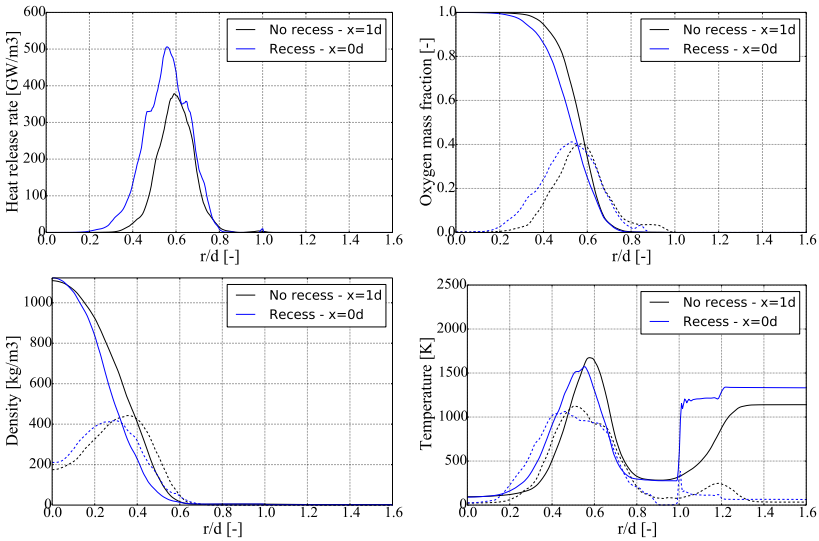

Fig. 35 No recess vs recess comparison. Radial profiles of heat release rate, oxygen mass fraction, temperature and density at the injector exit ($x = 0$ for case R and $x = 1d$ for case NR). − mean profiles, −− rms profiles.

increases the exit annular flow velocity. As a consequence, the resolved velocity fluctuations given by $k = \sqrt{u'^2 + v'^2 + w'^2}$, where u', v' and w' are velocity rms in each spatial directions, are also augmented in this region. They are plotted in Fig. 37a. As for the heat release rate, case R features much larger velocity fluctuations than case NR for r<0.6d. These velocity fluctuations are

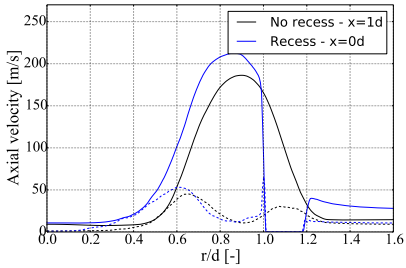

Fig. 36 No recess vs recess comparison. Radial profiles of axial velocity at the injector exit ($x = 0$ for case R and $x = 1d$ for case NR). − mean profiles, −− rms profiles.

found to be strongly correlated with the heat release. This is shown in Fig. 37b by plotting normalized heat release rate and velocity rms for cases R and NR. Normalized values ϕ are defined by $\phi_n = (\phi - \phi_{min})/(\phi_{max} - \phi_{min})$, where ϕ_{max} and ϕ_{min} are their maximum and minimum value for 0<r<1d. It suggests that the augmentation of velocity fluctuations enhances the turbulent mixing in the reactive layer and is at the origin of the augmented heat

release in the near injector region. Further downstream, the increase of heat release rate is a combined effect between the augmented turbulence and the augmented resolved flame surface because of the rapid destabilization of the inner jet.

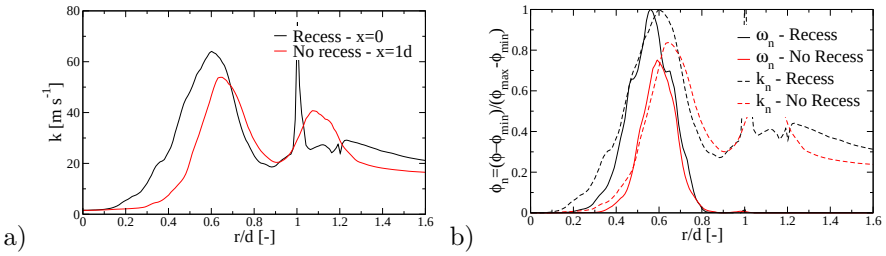

Fig. 37 No recess vs recess comparison. Radial profiles of (a) velocity rms $k = \sqrt{u'^2 + v'^2 + w'^2}$ and (b) normalized heat release rate ω_n and velocity rms k_n at the injector exit ($x = 0$ for case R and $x = 1d$ for case NR).

8 Conclusions

Large-Eddy Simulations (LES) of LOx/GH_2 coaxial injectors operating at high pressure and featuring a recessed LOx tube are shown in this article. The configurations correspond to the experimental Mascotte test-case A10 and C10 [4] at 10 bar and C60 [16] at 60 bar on which experimental tests with and without recess are available, in particular through experimental backlighting images for C60. For the latter, it was found experimentally that the inner dense LOx stream features large scale oscillations when the LOx tube is recessed.

For the case operating at 60 bar, mesh convergence is difficult to reach and a very fine grid is necessary for the natural instability of the recessed injector to properly develop. On the contrary, the cases at 10 bar, which do not feature such strong oscillations once the oxygen injector is recessed, show a more efficient mesh convergence. When compared with the experimental backlighting images, the simulation with a recessed injector at 60 bar shows a more intense dynamics of the inner jet. As a consequence the flame spreading rate is over-predicted by the LES. However, the sudden change for the inner jet dynamics as the injector is recessed is captured by the simulation. Cases at 10 bar qualitatively reproduce the experimental visualizations: the initial expansion of the flame is well retrieved and the maximum radius axial position is reasonably recovered for both cases.

A comparison with a flush mounted injector is performed for case C60. The recessed case features a much shorter flame. Its spreading rate is also strongly increased. One consequence is an important modification of the heat release rate distribution near the injector, nearly doubled up to 10 diameters. This behavior is of importance for combustion instabilities, since the flame response to an acoustic perturbation should be drastically changed by this geometrical

modification. It is found that the increase of heat release rate has two origins. First, because of the combustion occurring in the recess, the flow velocity at the injector exit is augmented. The turbulent mixing is consequently augmented which in turn increases the heat release. This phenomenon dominates at the injector exit. Further downstream, the increase of heat release is also due to an augmentation of the flame surface because of the enhanced dynamics of the recessed case, increasing the expansion of the flame. For cases A10 and C10, the increase of heat release is found to be essentially due to the augmentation of the flow velocity at the injector exit while the change of resolved flame surface is more limited than for case C60.

Acknowledgements

This work was granted access to the HPC resources of TGCC (CEA) and CINES made available by GENCI (Grand Equipement National de Calcul Intensif) under the allocation A0102B06176. A part of this work was performed using HPC resources from the mésocentre computing center of Ecole Centrale-Supélec and Ecole Normale Supérieure Paris-Saclay supported by CNRS and Région Ile-de-France.

Declarations

The author has no conflicts of interest to declare that are relevant to the content of this article.

A Statistical convergence in the recess for cases A10-R2, C10-R2 and C60-R3

Radial profiles of temperature and axial velocity are plotted for different averaging times in Fig. 38, 39 and 40 for cases A10-R2, C10-R2 and C60-R3, respectively. For all the cases, the different profiles are close from each other, suggesting the simulation is properly statistically converged in the recess.

B Mean fields for cases A10 and C10

Longitudinal slices of average temperature, density and oxygen mass fraction for cases A10 and C10 are shown in Fig. 41 and 42. As could have been expected from the lowered annular injection velocity, the flame for cases C10 penetrates further into the chamber than for cases A10. The recess of the LOx tube leads to a reduction of the flame length, for both cases. This is similar to the observations made on case C60. This reduction is associated with a modification of the heat release rate distribution in the chamber, as depicted in Fig. 43. For both cases, the heat release rate is augmented up to x≈8d. Differences between recessed and non recessed cases are less noticeable further downstream. The change of heat release due to the recess is lower than the

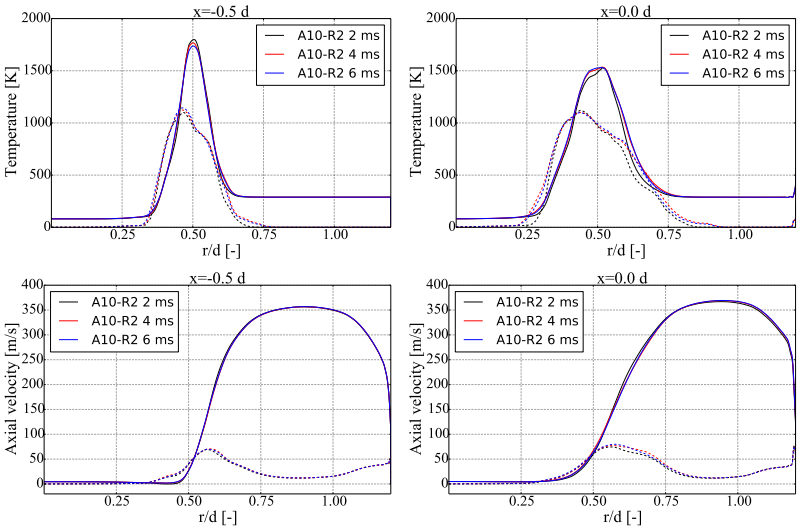

Fig. 38 Case A10-R2, statistical convergence in the recess. Radial profiles of axial velocity. − mean profiles, −− rms profiles.

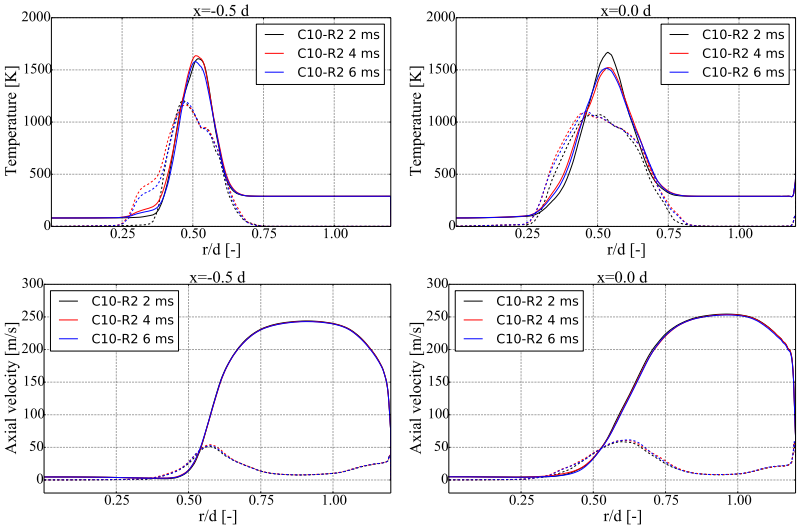

Fig. 39 Case C10-R2, statistical convergence in the recess. Radial profiles of axial velocity. − mean profiles, −− rms profiles.

one obtained at 60 bar, but an important growth of 70% is however measured at x=2d.

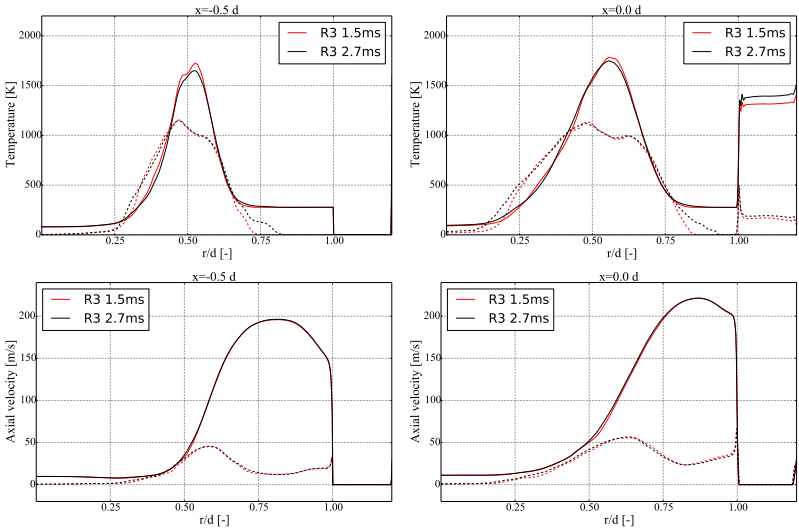

Fig. 40 Case C60-R3, statistical convergence in the recess. Radial profiles of axial velocity. − mean profiles, −− rms profiles.

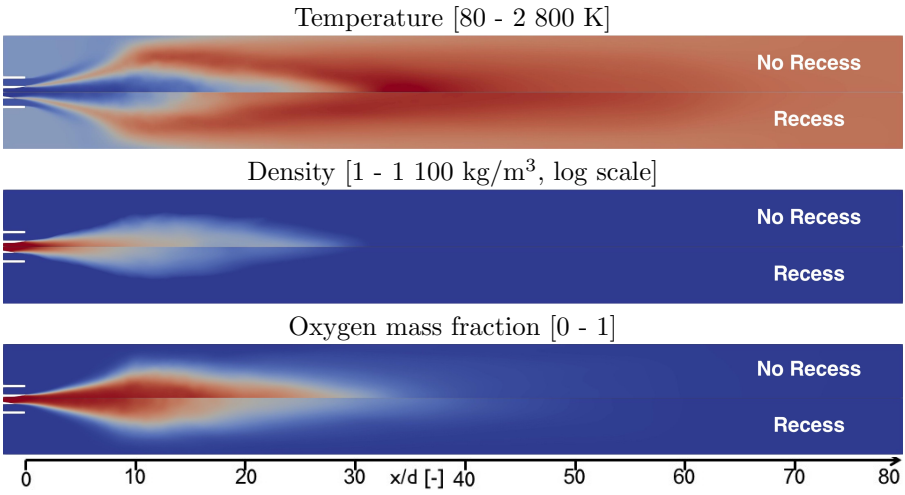

Fig. 41 Cases A10-NR and A10-R. Longitudinal slices of average temperature, density, oxygen mass fraction and axial velocity. Blue: minimum, red: maximum.

C Flame surface and heat release rate for cases A10 and C10

Following the procedure depicted in Sec. 7.3 and Eq. 4, resolved flame surfaces for cases A10 and C10 are plotted in Figs. 44a and 45a, respectively. Contrary to cases C60, the modification of the flame surface is here limited, and essentially corresponds to a one diameter shift of the curve once the injector is

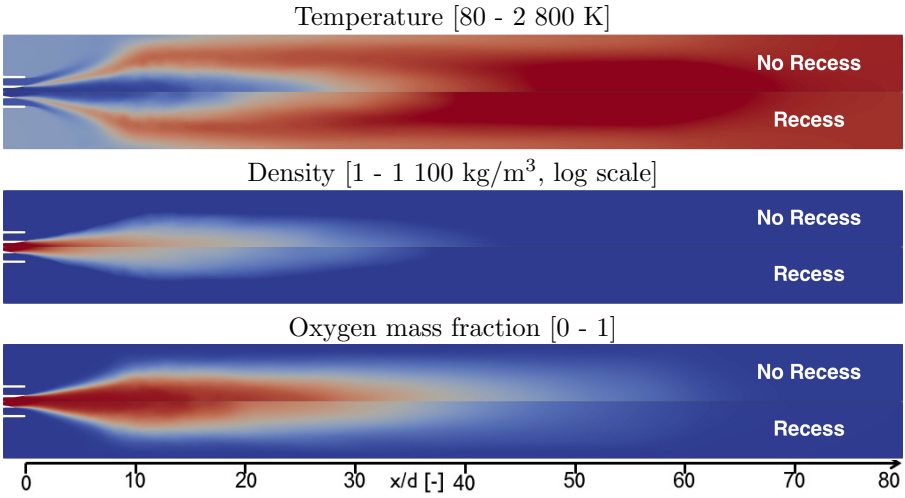

Fig. 42 Cases C10-NR and C10-R. Longitudinal slices of average temperature, density and oxygen mass fraction. Blue: minimum, red: maximum.

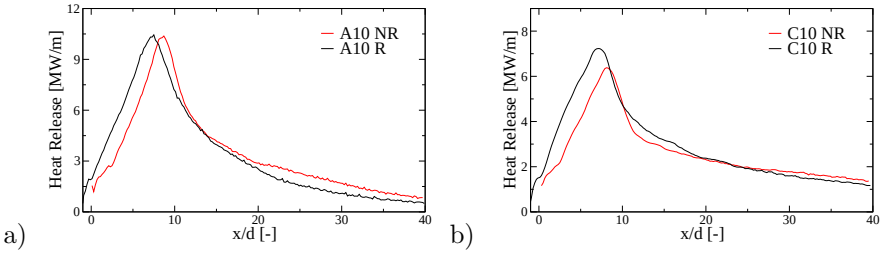

Fig. 43 Longitudinal profiles transversely integrated heat release per unit length for (a) cases A10 and (b) cases C10.

recessed. The change of heat release is thus provoked by a modification of the heat release per flame surface $\dot{q}_s$. This is shown in Figs. 44b and 45b, where $\dot{q}_s$ increases as the LOx injector is recessed. This is a consequence of the thermal expansion in the recess that augments velocity and turbulent mixing at the injector exit.

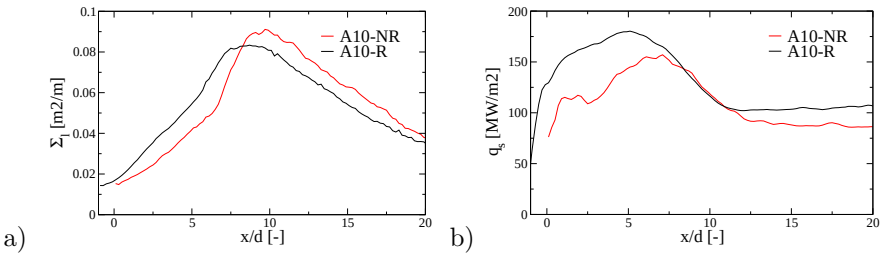

a) b)

Fig. 44 Cases A10-NR and A10-R. Longitudinal profile of (a) transversely integrated resolved flame surface per unit length and (b) transversely integrated heat release per resolved flame surface and per unit length.

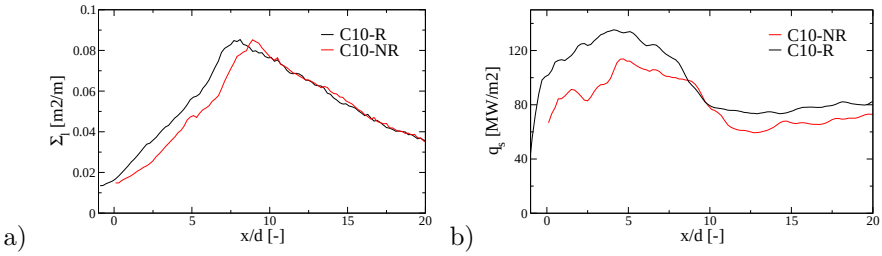

a) b)

Fig. 45 Cases C10-NR and C10-R. Longitudinal profile of (a) transversely integrated resolved flame surface per unit length and (b) transversely integrated heat release per resolved flame surface and per unit length.

References

[1] Schmitt, T.: Large-eddy simulations of the mascotte test cases operating at supercritical pressure. Flow, Turbulence and Combustion **105**, 159–189 (2020). https://doi.org/10.1007/s10494-019-00096-y

[2] Pelletier, M., Schmitt, T., Ducruix, S.: A multifluid taylor-galerkin methodology for the simulation of compressible multicomponent separate two-phase flows from subcritical to supercritical states. Computers & Fluids **206**, 104588 (2020). https://doi.org/10.1016/j.compfluid.2020.104588

[3] Habiballah, M., Orain, M., Grisch, F., Vingert, L., Gicquel, P.: Experimental Studies of High-Pressure Cryogenic Flames on the Mascotte Facility. Combustion Science and Technology **178**(1), 101–128 (2006). https://doi.org/10.1080/00102200500294486

[4] Kendrick, D., Herding, G., Scouflaire, P., Rolon, C., Candel, S.: Effects of a recess on cryogenic flame stabilization. Combustion and Flame **118**(3), 327–339 (1999). https://doi.org/10.1016/S0010-2180(98)00168-0

[5] Oefelein, J.C.: Mixing and Combustion of Cryogenic Oxygen-Hydrogen

Shear-Coaxial Jet Flames at Supercritical Pressure. Combustion Science and Technology **178**(1), 229–252 (2006). https://doi.org/10.1080/00102200500325322

[6] Zong, N., Yang, V.: Cryogenic Fluid Jets and Mixing Layers in Transcritical and Supercritical Environments. Combustion Science and Technology **178**(1), 193–227 (2006). https://doi.org/10.1080/00102200500287613

[7] Müller, H., Niedermeier, C.A., Matheis, J., Pfitzner, M., Hickel, S.: Large-eddy simulation of nitrogen injection at trans-and supercritical conditions. Physics of Fluids **28**(1), 015102 (2016). https://doi.org/10.1063/1.4937948

[8] Matheis, J., Hickel, S.: Multi-component vapor-liquid equilibrium model for les of high-pressure fuel injection and aplication to ecn spray a. International Journal of Multiphase Flow **99**, 294–311 (2018). https://doi.org/10.1016/j.ijmultiphaseflow.2017.11.001

[9] Zips, J., Traxinger, C., Breda, P., Pfitzner, M.: Assessment of presumed/-transported probability density function methods for rocket combustion simulations. Journal of Propulsion and Power **35**(4), 747–764 (2019). https://doi.org/10.2514/1.B37331

[10] Ma, P.C., Wu, H., Jaravel, T., Bravo, L., Ihme, M.: Large-eddy simulations of transcritical injection and auto-ignition using diffuse-interface method and finite-rate chemistry. Proceedings of the Combustion Institute **37**(3), 3303–3310 (2019). https://doi.org/10.1016/j.proci.2018.05.063

[11] Schmitt, T., Méry, Y., Boileau, M., Candel, S.: Large-eddy simulation of oxygen/methane flames under transcritical conditions. Proceedings of the Combustion Institute **33**(1), 1383–1390 (2011). https://doi.org/10.1016/j.proci.2010.07.036

[12] Zips, J., Müller, H., Pfitzner, M.: Efficient thermo-chemistry tabulation for non-premixed combustion at high-pressure conditions. Flow, Turbulence and Combustion **101**(3), 821–850 (2018). https://doi.org/10.1007/s10494-018-9932-4

[13] Hakim, L., Ruiz, A., Schmitt, T., Boileau, M., Staffelbach, G., Ducruix, S., Cuenot, B., Candel, S.: Large eddy simulations of multiple transcritical coaxial flames submitted to a high-frequency transverse acoustic modulation. Proceedings of the Combustion Institute **35**(2), 1461–1468 (2015). https://doi.org/10.1016/j.proci.2014.05.142

[14] Urbano, A., Selle, L., Staffelbach, G., Cuenot, B., Schmitt, T., Ducruix, S., Candel, S.: Exploration of combustion instability triggering using large

eddy simulation of a multiple injector liquid rocket engine. Combustion and Flame **169**, 129–140 (2016). https://doi.org/10.1016/j.combustflame.2016.03.020

[15] Schmitt, T., Staffelbach, G., Ducruix, S., Gröning, S., Hardi, J., Oschwald, M.: Large-eddy simulations of a sub-scale liquid rocket combustor: Influence of fuel injection temperature on thermo-acoustic stability. In: 7TH European Conference for Aeronautics and Aerospace Sciences (EUCASS) (2017). https://doi.org/10.13009/EUCASS2017-352

[16] Candel, S., Juniper, M., Single, G., Scouflaire, P., Rolon, C.: Structure and dynamics of cryogenic flames at supercritical pressure. Combustion Science and Technology **178**, 161–192 (2006). https://doi.org/10.1080/00102200500292530

[17] Juniper, M.P., Candel, S.M.: The Stability of Ducted Compound Flows and Consequences for the Geometry of Coaxial Injectors. Journal of Fluid Mechanics **482**, 257–269 (2003). https://doi.org/10.1017/S0022112003004075

[18] Vingert, L., Habiballah, M., Vuillermoz, P., Zurbach, S.: MASCOTTE, a Test Facility for Cryogenic Combustion Research at High Pressure. In: 51st International Astronautical Congress, Rio de Janeiro, Brazil (2000). https://www.osti.gov/etdeweb/biblio/20222846

[19] Lee, L.L., Starling, K.E., Chung, T.H., Ajlan, M.: Generalized multiparameters corresponding state correlation for polyatomic, polar fluid transport properties. Industrial and Chemical Engineering Research **27**, 671–679 (1988). https://doi.org/10.1021/ie00076a024

[20] Nicoud, F., Ducros, F.: Subgrid-scale stress modelling based on the square of the velocity gradient. Flow, Turbulence and Combustion **62**(3), 183–200 (1999). https://doi.org/10.1023/A:1009995426001

[21] Soave, G.: Equilibrium constants from a modified redlich-kwong equation of state. Chemical Engineering Science **27**, 1197–1203 (1977). https://doi.org/10.1016/0009-2509(72)80096-4

[22] Poling, B.E., Prausnitz, J.M., O'Connel, J.P.: The Properties of Gases and Liquids, 5th edn. McGraw-Hill Education, New York (2001)

[23] Moureau, V., Lartigue, G., Sommerer, Y., Angelberger, C., Colin, O., Poinsot, T.: Numerical methods for unsteady compressible multi-component reacting flows on fixed and moving grids. Journal of Computational Physics **202**(2), 710–736 (2005). https://doi.org/10.1016/j.jcp.2004.08.003

[24] Schönfeld, T., Rudgyard, M.: Steady and unsteady flows simulations using the hybrid flow solver avbp. AIAA Journal **37**(11), 1378–1385 (1999). https://doi.org/10.2514/2.636

[25] Colin, O., Rudgyard, M.: Development of high-order taylor-galerkin schemes for unsteady calculations. Journal of Computational Physics **162**(2), 338–371 (2000). https://doi.org/10.1006/jcph.2000.6538

[26] Okong'o, N., Bellan, J.: Consistent boundary conditions for multicompoment real gas mixtures based on characteristic waves. Journal of Computational Physics **176**, 330–344 (2002). https://doi.org/10.1006/jcph.2002.6990

[27] Schmitt, P., Poinsot, T.J., Schuermans, B., Geigle, K.: Large-eddy simulation and experimental study of heat transfer, nitric oxide emissions and combustion instability in a swirled turbulent high pressure burner. Journal of Fluid Mechanics **570**, 17–46 (2007). https://doi.org/10.1017/S0022112006003156

[28] Jaegle, F., Cabrit, O., Mendez, S., Poinsot, T.: Implementation methods of wall functions in cell-vertex numerical solvers. Flow, Turbulence and Combustion **85**(2), 245–272 (2010). https://doi.org/10.1007/s10494-010-9276-1

[29] Daviller, G., Brebion, M., Xavier, P., Staffelbach, G., Müller, J.-D., Poinsot, T.: A mesh adaptation strategy to predict pressure losses in les of swirled flows. Flow, Turbulence and Combustion **99**, 93–118 (2017). https://doi.org/10.1007/s10494-017-9808-z

[30] Dapogny, C., Dobrzynski, C., Frey, P.: Three-dimensional adaptive domain remeshing, implicit domain meshing, and applications to free and moving boundary problems. Journal of computational Physics **262**, 358–378 (2014). https://doi.org/10.1016/j.jcp.2014.01.005

[31] Moureau, V., Domingo, P., Vervisch, L.: From large-eddy simulation to direct numerical simulation of a lean premixed swirl flame: Filtered laminar flame-pdf modeling. Combustion and Flame **158**(7), 1340–1357 (2011). https://doi.org/10.1016/j.combustflame.2010.12.004

[32] Juniper, M., Tripathi, A., Scouflaire, P., Rolon, J., Candel, S.: Structure of cryogenic flames at elevated pressures. Proceedings of the Combustion Institute **28**(1), 1103–1110 (2000). https://doi.org/10.1016/S0082-0784(00)80320-3

[33] Veynante, D., Vervisch, L.: Turbulent combustion modeling. Progress in Energy and Combustion Science **28**, 193–266 (2002). https://doi.org/10.1016/S0360-1285(01)00017-X